8-27-2015

Direct Regularization from Co-Registered Anatomical Images for MRI-Guided Near-Infrared Spectral Tomographic Image Reconstruction

Limin Zhang
Dartmouth College

Yan Zhao
Dartmouth College

Shudong Jiang
Dartmouth College

Brian W. Pogue
Dartmouth College

Keith Paulsen
Dartmouth College

Biomedical Optics EXPRESS

Direct regularization from co-registered anatomical images for MRI-guided near-infrared spectral tomographic image reconstruction

Limin Zhang,[1,2,3] Yan Zhao,[1] Shudong Jiang,[1] Brian W. Pogue,[1] and Keith D. Paulsen[1,*]

[1]*Thayer School of Engineering, Dartmouth College, Hanover NH 03755, USA*
[2]*College of Precision Instrument and Optoelectronics Engineering, Tianjin University, Tianjin 300072, China*
[3]*Tianjin Key Laboratory of Biomedical Detecting Techniques and Instrument, Tianjin 300072, China*
[*]*keith.d.paulsen@dartmouth.edu*

Abstract: Combining anatomical information from high resolution imaging modalities to guide near-infrared spectral tomography (NIRST) is an efficient strategy for improving the quality of the reconstructed spectral images. A new approach for incorporating image information directly into the inversion matrix regularization was examined using Direct Regularization from Images (DRI), which encodes the gray-scale data into the NIRST image reconstruction problem. This process has the benefit of eliminating user intervention such as image segmentation of distinct regions. Specifically, the Dynamic Contrast Enhanced Magnetic Resonance (DCE-MR) image intensity value differences within the anatomical image were used to implement an exponentially-weighted regularization function between the image pixels. The algorithm was validated using simulated reconstructions with noise, and the results showed that spatial resolution and robustness of the reconstructed images were significantly improved by appropriate choice of the regularization weight parameters. The proposed approach was also tested on *in vivo* breast data acquired in a recent clinical trial combining NIRST / MRI for cancer tumor characterization. Relative to the standard "no priors" diffuse recovery, the contrast of the tumor to the normal surrounding tissue increased from 2.4 to 3.6, and the difference between the tumor size segmented from DCE-MR images and reconstructed optical images decreased from 18% to 6%, while there was an overall decrease in surface artifacts.

OCIS codes: (170.3880) Medical and biological imaging; (100.3010) Image reconstruction techniques; (170.6960) Tomography.

References and links

1. D. A. Boas, D. H. Brooks, E. L. Miller, C. A. DiMarzio, M. Kilmer, R. J. Gaudette, and Q. Zhang, "Imaging the body with diffuse optical tomography," IEEE Signal Process. Mag. **18**(6), 57–75 (2001).
2. M. L. Flexman, F. Vlachos, H. K. Kim, S. R. Sirsi, J. Huang, S. L. Hernandez, T. B. Johung, J. W. Gander, A. R. Reichstein, B. S. Lampl, A. Wang, M. A. Borden, D. J. Yamashiro, J. J. Kandel, and A. H. Hielscher, "Monitoring early tumor response to drug therapy with diffuse optical tomography," J. Biomed. Opt. **17**(1), 016014 (2012).
3. C. M. Carpenter, B. W. Pogue, S. Jiang, H. Dehghani, X. Wang, K. D. Paulsen, W. A. Wells, J. Forero, C. Kogel, J. B. Weaver, S. P. Poplack, and P. A. Kaufman, "Image-guided optical spectroscopy provides molecular-specific information in vivo: MRI-guided spectroscopy of breast cancer hemoglobin, water, and scatterer size," Opt. Lett. **32**(8), 933–935 (2007).
4. S. R. Arridge, "Optical tomography in medical imaging," Inverse Probl. **15**(2), R41–R93 (1999).
5. B. W. Pogue, X. Song, T. D. Tosteson, T. O. McBride, S. Jiang, and K. D. Paulsen, "Statistical analysis of nonlinearly reconstructed near-infrared tomographic images: Part I--Theory and simulations," IEEE Trans. Med. Imaging **21**(7), 755–763 (2002).

#239691 Received 5 May 2015; revised 16 Jul 2015; accepted 17 Aug 2015; published 27 Aug 2015

6. Q. Fang, R. H. Moore, D. B. Kopans, and D. A. Boas, "Compositional-prior-guided image reconstruction algorithm for multi-modality imaging," Biomed. Opt. Express **1**(1), 223–235 (2010).
7. Q. Fang, S. A. Carp, J. Selb, G. Boverman, Q. Zhang, D. B. Kopans, R. H. Moore, E. L. Miller, D. H. Brooks, and D. A. Boas, "Combined optical imaging and mammography of the healthy breast: optical contrast derived from breast structure and compression," IEEE Trans. Med. Imaging **28**(1), 30–42 (2009).
8. Q. Zhu, N. Chen, and S. H. Kurtzman, "Imaging tumor angiogenesis by use of combined near-infrared diffusive light and ultrasound," Opt. Lett. **28**(5), 337–339 (2003).
9. Q. Zhang, T. J. Brukilacchio, A. Li, J. J. Stott, T. Chaves, E. Hillman, T. Wu, M. Chorlton, E. Rafferty, R. H. Moore, D. B. Kopans, and D. A. Boas, "Coregistered tomographic x-ray and optical breast imaging: initial results," J. Biomed. Opt. **10**(2), 024033 (2005).
10. P. Hiltunen, S. J. Prince, and S. Arridge, "A combined reconstruction-classification method for diffuse optical tomography," Phys. Med. Biol. **54**(21), 6457–6476 (2009).
11. B. W. Pogue, H. Zhu, C. Nwaigwe, T. O. McBride, U. L. Osterberg, K. D. Paulsen, and J. F. Dunn, "Hemoglobin imaging with hybrid magnetic resonance and near-infrared diffuse tomography," Adv. Exp. Med. Biol. **530**, 215–224 (2003).
12. M. Guven, B. Yazici, X. Intes, and B. Chance, "Diffuse optical tomography with a priori anatomical information," Phys. Med. Biol. **50**(12), 2837–2858 (2005).
13. A. Li, G. Boverman, Y. Zhang, D. Brooks, E. L. Miller, M. E. Kilmer, Q. Zhang, E. M. Hillman, and D. A. Boas, "Optimal linear inverse solution with multiple priors in diffuse optical tomography," Appl. Opt. **44**(10), 1948–1956 (2005).
14. P. K. Yalavarthy, B. W. Pogue, H. Dehghani, C. M. Carpenter, S. Jiang, and K. D. Paulsen, "Structural information within regularization matrices improves near infrared diffuse optical tomography," Opt. Express **15**(13), 8043–8058 (2007).
15. V. Ntziachristos, A. G. Yodh, M. D. Schnall, and B. Chance, "MRI-guided diffuse optical spectroscopy of malignant and benign breast lesions," Neoplasia **4**(4), 347–354 (2002).
16. Y. Lin, D. Thayer, O. Nalcioglu, and G. Gulsen, "Tumor characterization in small animals using magnetic resonance-guided dynamic contrast enhanced diffuse optical tomography," J. Biomed. Opt. **16**(10), 106015 (2011).
17. B. Brooksby, S. Jiang, H. Dehghani, B. W. Pogue, K. D. Paulsen, J. Weaver, C. Kogel, and S. P. Poplack, "Combining near-infrared tomography and magnetic resonance imaging to study in vivo breast tissue: implementation of a Laplacian-type regularization to incorporate magnetic resonance structure," J. Biomed. Opt. **10**(5), 051504 (2005).
18. B. Brooksby, B. W. Pogue, S. Jiang, H. Dehghani, S. Srinivasan, C. Kogel, T. D. Tosteson, J. Weaver, S. P. Poplack, and K. D. Paulsen, "Imaging breast adipose and fibroglandular tissue molecular signatures by using hybrid MRI-guided near-infrared spectral tomography," Proc. Natl. Acad. Sci. U.S.A. **103**(23), 8828–8833 (2006).
19. F. S. Azar, K. Lee, A. Khamene, R. Choe, A. Corlu, S. D. Konecky, F. Sauer, and A. G. Yodh, "Standardized platform for coregistration of nonconcurrent diffuse optical and magnetic resonance breast images obtained in different geometries," J. Biomed. Opt. **12**(5), 051902 (2007).
20. C. B. Shaw and P. K. Yalavarthy, "Prior image-constrained ℓ (1)-norm-based reconstruction method for effective usage of structural information in diffuse optical tomography," Opt. Lett. **37**(20), 4353–4355 (2012).
21. B. A. Brooksby, H. Dehghani, B. W. Pogue, and K. D. Paulsen, "Near-infrared (NIR) tomography breast image reconstruction with a priori structural information from MRI: algorithm development for reconstructing heterogeneities," IEEE J. Sel. Top. Quantum Electron. **9**(2), 199–209 (2003).
22. R. W. Holt, S. Davis, and B. W. Pogue, "Regularization functional semi-automated incorporation of anatomical prior information in image-guided fluorescence tomography," Opt. Lett. **38**(14), 2407–2409 (2013).
23. B. W. Pogue, S. C. Davis, F. Leblond, M. A. Mastanduno, H. Dehghani, and K. D. Paulsen, "Implicit and explicit prior information in near-infrared spectral imaging: accuracy, quantification and diagnostic value," Philos. Trans. A Math Phys. Eng. Sci. 369(1955), 4531–4557 (2011).
24. B. W. Pogue, S. C. Davis, X. Song, B. A. Brooksby, H. Dehghani, and K. D. Paulsen, "Image analysis methods for diffuse optical tomography," J. Biomed. Opt. **11**(3), 033001 (2006).
25. H. Dehghani, M. E. Eames, P. K. Yalavarthy, S. C. Davis, S. Srinivasan, C. M. Carpenter, B. W. Pogue, and K. D. Paulsen, "Near infrared optical tomography using NIRFAST: Algorithm for numerical model and image reconstruction," Commun. Numer. Methods Eng. **25**(6), 711–732 (2009).
26. M. A. Mastanduno, F. El-Ghussein, S. Jiang, R. Diflorio-Alexander, X. Junqing, Y. Hong, B. W. Pogue, and K. D. Paulsen, "Adaptable near-infrared spectroscopy fiber array for improved coupling to different breast sizes during clinical MRI," Acad. Radiol. **21**(2), 141–150 (2014).
27. F. El-Ghussein, M. A. Mastanduno, S. Jiang, B. W. Pogue, and K. D. Paulsen, "Hybrid photomultiplier tube and photodiode parallel detection array for wideband optical spectroscopy of the breast guided by magnetic resonance imaging," J. Biomed. Opt. **19**(1), 011010 (2013).
28. M. A. Mastanduno, J. Xu, F. El-Ghussein, S. Jiang, H. Yin, Y. Zhao, K. E. Michaelsen, K. Wang, F. Ren, B. W. Pogue, and K. D. Paulsen, "Sensitivity of MRI-guided near-infrared spectroscopy clinical breast exam data and its impact on diagnostic performance," Biomed. Opt. Express **5**(9), 3103–3115 (2014).

#239691 Received 5 May 2015; revised 16 Jul 2015; accepted 17 Aug 2015; published 27 Aug 2015

29. C. M. Carpenter, S. Srinivasan, B. W. Pogue, and K. D. Paulsen, "Methodology development for three-dimensional MR-guided near infrared spectroscopy of breast tumors," Opt. Express **16**(22), 17903–17914 (2008).

1. Introduction

Near-infrared spectral tomography (NIRST) is a non-invasive biomedical imaging modality that can be utilized to measure physiologically relevant optical properties of tissue and has been of considerable research interest for applications in brain imaging and breast cancer characterization [1, 2]. As a functional imaging tool, NIRST has the advantage of directly measuring hemoglobin and its oxygenation state as well as water, lipids, collagen and scattering features [3]. Yet, the technique suffers from low spatial resolution due to the strongly scattering nature of NIR light propagation in tissue, leading to an ill-posed inverse problem [4, 5]. The modest spatial resolution is well recognized and studied in NIRST *in vivo* breast imaging, where light sampling on the surface is used to recover images of heterogeneous tissue at depth. At present, significant effort has been devoted to improving the resolution of the NIRST through image-guided spectroscopy [6–10] – an efficient strategy which combines segmented anatomical information obtained from high resolution imaging modalities to directly guide and improve the recovery of optical properties, through pre-definition of homogenous regions to estimate NIR parameters [11–16]. An alternative approach implements a spatially encoded regularization, where co-registered image information is applied in a pre-defined way, such as through a Laplacian filter or a depth dependent function [17, 18]. In this study, gray scale levels from a co-registered DCE-MR image were incorporated into NIRST of the breast.

In MRI-guided NIRST applications, previous work investigated image reconstruction in an indirect two-step procedure [19]. First, high resolution anatomical images provided by MRI were segmented into a small number of sub-domains with assumed homogeneous or constant optical properties representing the major tissues types. For breast imaging, tissues can be readily segmented into adipose, fibroglandular and suspicious regions. Then, the prior structural information from MRI imposed either a hard or a soft constraint on the image reconstruction process [20, 21]. If the optical properties within an identified region were forced to be uniform, the constraint was often called a "hard prior". The notable advantage of using a hard-prior scheme is the dramatic reduction in the total number of unknowns alleviating the ill-posedness of the inversion by reducing the number of unknowns to the few identified homogenous volumes. This process has the peripheral benefit of significantly enhancing NIRST accuracy within the localized regions. However, its stability is critically dependent on the accuracy of the structural priors derived from the co-registered image, and performance is degraded when incomplete or distorted structural priors are employed. Schemes based on "soft priors" do not require optical-property boundaries to coincide with the MR-defined boundaries; therefore, they allow changes across boundaries, and reduce the likelihood that spatial biases will be introduced during the inversion process. Other methods that encode some uniformity into the inversion are also possible such as total variation minimization or Laplacian smoothing. However, the hard and soft prior approaches that have been tested require user input to guide the image segmentation involved. Unfortunately, segmentation can be time consuming for the user, especially when the tissues of interest are large, and is prone to errors, for example, when identifying tumor boundaries if the radiological or anatomical training of the user is not sufficient. Thus, a direct reconstruction method, which implicitly incorporates the anatomical information into the inversion problem without user intervention, would dramatically reduce processing time and expand the potential of multimodal imaging such as MRI-NIRST by fully automating the image reconstruction process. In reference [6], a novel soft prior approach was introduced which combines the segmentation of specific tissue types with their encoding into a regularization matrix that has similar approximate form to the scheme presented here. However, a key

#239691 Received 5 May 2015; revised 16 Jul 2015; accepted 17 Aug 2015; published 27 Aug 2015

difference here is the realization of a regularization functional which does not require any human intervention (e.g., no segmentation or other prior decisions about tissue composition).

In this paper, we demonstrate a Direct Regularization Imaging (DRI) method for MRI-guided Near-Infrared Spectroscopy Tomography. The approach was previously demonstrated for fluorescence recovery of probe concentrations in tumors [22], but has not been considered in the setting of endogenous absorption and scatter imaging. In this method, the gray scale values of the MRI images directly regularize the inverse problem avoiding the need for segmenting image structure and making undue assumptions about the imaging domain. The approach is particularly relevant for MRI-coupled imaging, since multiple types of weighted images are available for the regularization and mesh creation processes. We evaluate the performance of our algorithm in numerical simulations, and compare the results with the standard "no priors" diffuse recovery scheme. The numerical studies show that the proposed method obtains significantly better image resolution and quality compared with the no prior method. Reconstructed optical property images acquired from a patient with breast cancer are shown using DCE-MR images as the source of the prior information.

2. Methods

2.1 Theory

The goal of NIRST is to reconstruct spatial maps of optical properties from fluence measurements on tissue surfaces using a forward model of the photon propagation in the scattering medium. For the forward problem, the solution usually relies on numerical techniques such as the finite element method (FEM) to solve a model of the diffusion approximation to the radiative transfer equation. The inverse problem can be posed as a least-squares multi-parametric optimization which recovers the optical properties at each node of the FEM mesh representing the tissue, by minimizing the difference between measured and computed data. Since the inverse problem is ill-posed, and in general, is often underdetermined, regularization is necessary to stabilize the reconstruction procedure. Regularization techniques are generally based on the Tikhonov framework given by the formulation

$$S(x) = \left\| f(x) - d \right\|_2^2 + \lambda \left\| Lx \right\|_2^2 \tag{1}$$

where x is an array of free parameters, f is the simulated data from the forward model governing the behavior of a system, d is the measured data, λ is known as Tikhonov regularization parameter or weighting coefficient which serves to determine the relative weight accorded to each of the two terms in Eq. (1), and L is some regularization matrix. The first term in Eq. (1), defined as model error, represents the deviation of the observed image from the model observation. The second term, defined as the prior error, is the deviation of the solution image from the prior knowledge. For the standard "no priors" diffuse method, the regularization matrix $\boldsymbol{L}$ is set to the identity matrix, which applies the same weight to the values at all nodes within the imaging domain. For the soft prior method, a Laplacian or Helmholtz operator can also be used [23].

Here, a regularization scheme is applied which directly encodes information about the structural images, rather than enforcing uniformity within manually-segmented regions. It is referred to as the DRI method and constrains FEM nodes according to their corresponding grayscale value differences within the coregistered companion image volume. In this case, the regularization matrix operator can be written as:

#239691 Received 5 May 2015; revised 16 Jul 2015; accepted 17 Aug 2015; published 27 Aug 2015

$$L_{ij} = \begin{cases} 1 & i = j \\ -\frac{1}{M_i} \exp\left(-\frac{\left|\gamma_i - \gamma_j\right|^2}{2\sigma_g} \right), & otherwise \end{cases} \quad (2)$$

where γ is the anatomical image grayscale value which corresponds to a particular FEM node (in this work, grayscale values were normalized to the maximum within the image), σ_g is the characteristic grayscale difference over which to apply regularization, and M_i is a normalization factor chosen for each row.

By performing an iterative Gauss-Newton reconstruction method through Eq. (1), the general update equation for the underdetermined form can be expressed as

$$\Delta x_k = (J_k^T J_k + \lambda L^T L)^{-1} J^T (d - f(x_{k-1})) \quad (3)$$

where Δx_k is the update to the parameters; J_k is the Jacobian matrix which is the derivative of the measurements, $f(x)$, with respect to the optical property parameters of interest at the k-th iteration, and has the dimension of $M \times N$, M is the number of measurements, and N is the number of parameters, x; the superscript T denotes the transpose, $f(x_{k-1})$ is the forward solution using the estimated parameters form the $k-1$ iteration.

In order to quantitatively compare the images reconstructed from different approaches, the absolute bias error was calculated as [24]

$$\left|Bias\ \ Error\right| = \frac{\sum_i^N \left|\mu_i - \mu_i^o\right|}{N} \quad (4)$$

where μ_i is the recovered optical coefficient at pixel i for the image reconstruction, μ_i^0 is the true value of the optical coefficient at the same location, and N is the number of pixels.

1.2 Numerical simulation

Figure 1 show a 2D circular simulation phantom generated from a finite-element model. The diameters and the center coordinates of the phantom and inclusion were 80 & 10 mm, and (50, 50) and (65, 35), respectively. The absorption coefficient (μ_a) inside of the inclusion was 0.02mm^{-1}, which was twice the value outside of the inclusion, 0.01mm^{-1}, while the reduced scattering coefficient (μ_s') of the entire phantom was 1.0mm^{-1} (Fig. 1(a)). As shown in Fig. 1(b), the contrast of the gray values of the inclusion to the remaining area of the phantom was 1.6 to simulate the type of DCE-MRI contrast commonly observed. For this simulation, 16 co-located source detector positions were placed with regular angular distribution around the phantom. For each source illumination, data was collected at 16 detector locations which lead to a total of 256 measurements. Fig. 1(c) depicts a fine mesh consisting of 7909 nodes that correspond to 155503 triangular elements. By using a diffusion model and adding 5% noise, the simulated data was generated using NIRFAST [25]. Image reconstruction was performed on a much coarser mesh having a total of 2001 nodes corresponding to 3867 triangular elements. (Fig. 1(d)). Images were reconstructed based on a reconstruction pixel basis of 30 × 30, and the algorithm was iterated until the difference between the forward data and the reconstructed data did not decrease by more than 2% relative to the previous iteration

#239691 Received 5 May 2015; revised 16 Jul 2015; accepted 17 Aug 2015; published 27 Aug 2015

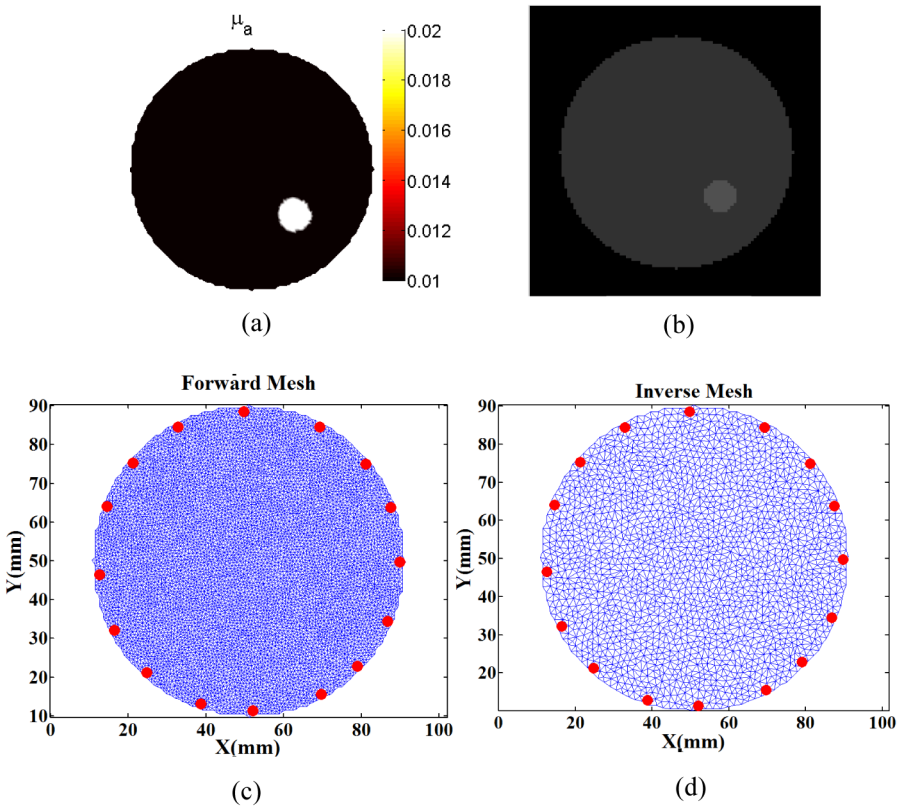

Fig. 1. (a) The true optical absorption distribution with $\mu_a = 0.02\text{mm}^{-1}$ in target region and $\mu_a = 0.01\text{mm}^{-1}$ in the background, (b) the gray value distribution with 80 in target region and 50 in the background (c) fine mesh for the forward problem, (d) coarse mesh for the inverse problem, with 16 co-located source detector positions placed at regular angles around the object. Red dots indicate the source-detector locations.

1.3 Patient imaging

Data was collected through an imaging protocol for human subject examination approved by the Committee for the Protection of Human Subjects at Dartmouth College and at Xijing Hospital. Written consent was obtained after the protocol was explained to a subject. The subject was positioned into an adjustable triangular breast interface (that couples to a standard MR breast coil) while prone on the MR examination table. Sixteen fiber bundles were held on the breast interface and used to deliver and detect the lights signals [24]. MR fiducial markers were placed in the plane of each set of fibers and were used to co-register the optical and MR images. The details of the MRI guided NIRST system have been reported previously [26–28]. In this system, six frequency domain (FD) and three continuous-wavelength (CW) laser diodes operating in the wavelength range of 660-950nm, were used as the light sources. Through a custom-made optical switch, the breast was illuminated sequentially at sixteen source positions. During each source illumination, the other 15 fibers detected the transmitted and diffused light with photomultiplier tubes and photodiodes. Optical and MR data were acquired concurrently with data acquisition times of 15 and 30 minutes, respectively.

The open source software Nirview and Nirfast (http://www.dartmouth.edu/~nir/nirfast/) were used to generate the 3D mesh. To perform image reconstruction, the mesh was created from the T1-weighted MRI volume, while the gray value information was obtained from the DCE-MRI volume. The MR images for the patient are shown in Section 3. A pixel basis of 25 × 25 × 25 was used in the inversion with a maximum iteration number of 5.

#239691 Received 5 May 2015; revised 16 Jul 2015; accepted 17 Aug 2015; published 27 Aug 2015

3. Results

3.1 Numerical simulation

Figure 2 shows the absorption coefficient recovered from simulated data using no prior and

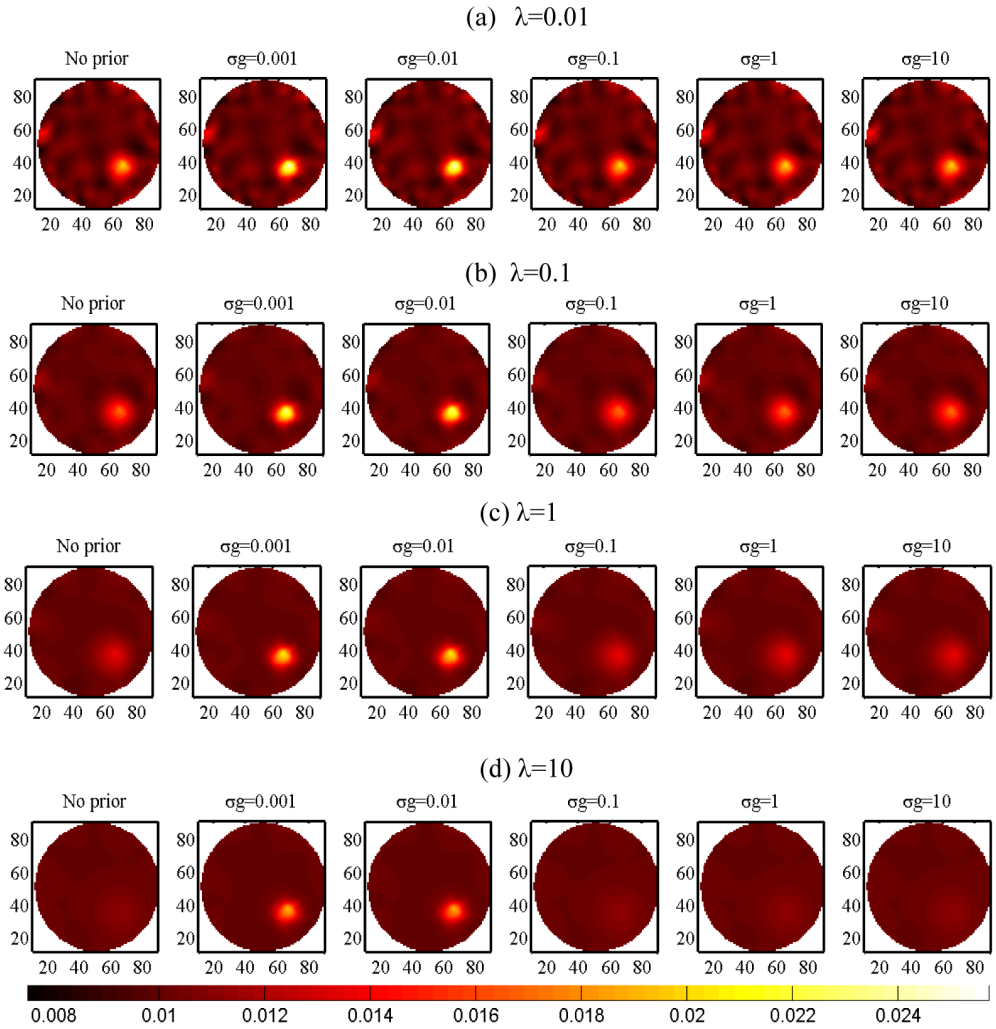

Fig. 2. The reconstructed absorption coefficient images from simulated data are shown, using no prior (left column) and DRI methods with a series of parameters λ=0.01(a), 0.1(b), 1(c), 10(d) and σ_g=0.001, 0.01, 0.1, 1, 10 (in each column to the right). The unit of x and y axes is mm.

DRI reconstruction approaches. To demonstrate the effect of varying regularization parameter, λ, for the no prior method, a series of values - 0.01, 0.1, 1, and 10 - were selected to recover the images of the absorption coefficient. The same series of regularization parameters were also used in the DRI approach, but were combined with the other parameter, σ_g - 0.001, 0.01, 0.1, 1 and 10. The reconstructed contrast decreased while the noise was efficiently suppressed when λ increased from 0.01 to 10. However, high reconstruction contrast occurred no matter which regularization parameter was selected for DRI with small σ_g (0.001, 0.01). Figure 3 shows cross-section profiles through the center of the inclusion and along the X-axis as a function of σ_g for different λ values. When small σ_g and λ were chosen, the peak value of the reconstruction overestimated the true absorption coefficient in the

#239691 Received 5 May 2015; revised 16 Jul 2015; accepted 17 Aug 2015; published 27 Aug 2015

inclusion, (see red and light blue lines in Fig. 3(a) and 3(b)). Interestingly, when the value of σ_g was large (see dark blue and black lines), the results were almost identical for both the DRI and no prior methods. This outcome suggests that choosing an optimum σ_g is crucial for the DRI method. In addition, the reconstructed images with DRI were notably superior when λ was large and σ_g was small. In this case, they are quantitatively accurate and the recovery was a robust representation of the true image.

To further investigate the effectiveness of the DRI approach, a negative control was also evaluated. In this test, the absorption coefficient inside of the inclusion was set to be the same as that of the background ($\mu_a = 0.01\text{mm}^{-1}$), while the gray-scale contrast inside and outside of the inclusion remained unchanged. Since for $\lambda = 10$, the DRI method results were optimal with appropriate σ_g, the negative control was evaluated with $\lambda = 10$ and $\sigma_g = 0.001$, 0.01, 0.1, 1, 10. Figure 3(e) presents the cross sectional profiles from these reconstructed results. Small error within the original optical properties was observed independently of the σ_g selection, indicating that the optical properties can be faithfully estimated with the DRI approach.

In order to investigate the spatial resolution attained with the algorithm, we calculated the full-width-at-half-maximum (FWHM) of the inclusion from the cross sectional image profiles and the results are shown in Fig. 4(a). For the no priors case, the measured FWHM increased as the value of λ increased, indicating that the spatial resolution of reconstructed images decreased, whereas, the DRI approach resulted in substantially increased spatial resolution when the value of σ_g was decreased. Specifically, when the value of σ_g was smaller than 0.01 and λ>0.01, the FWHM values were almost the same as the size of the true target. For larger σ_g, the measured FWHM values were the same as the no prior results.

Figure 4(b) illustrates the absolute bias error for the entire image. The larger regularization parameters resulted in small absolute bias error in all cases. In addition, the bias error decreased as the value of σ_g decreased. This finding suggests that the image noise can be efficiently dampened when small σ_g is chosen. Indeed, the error of the DRI approach was approximately the same as that with no priors when $\sigma_g > 0.1$.

In addition, to test the DRI approach under multi-inclusion conditions, a phantom with two different sizes inclusions and the same optical properties and gray values as the previous case were reconstructed. The results show that the DRI approach can successfully recover images with two inclusions, and the selection of parameters is consistent with the single inclusion case.

#239691 Received 5 May 2015; revised 16 Jul 2015; accepted 17 Aug 2015; published 27 Aug 2015

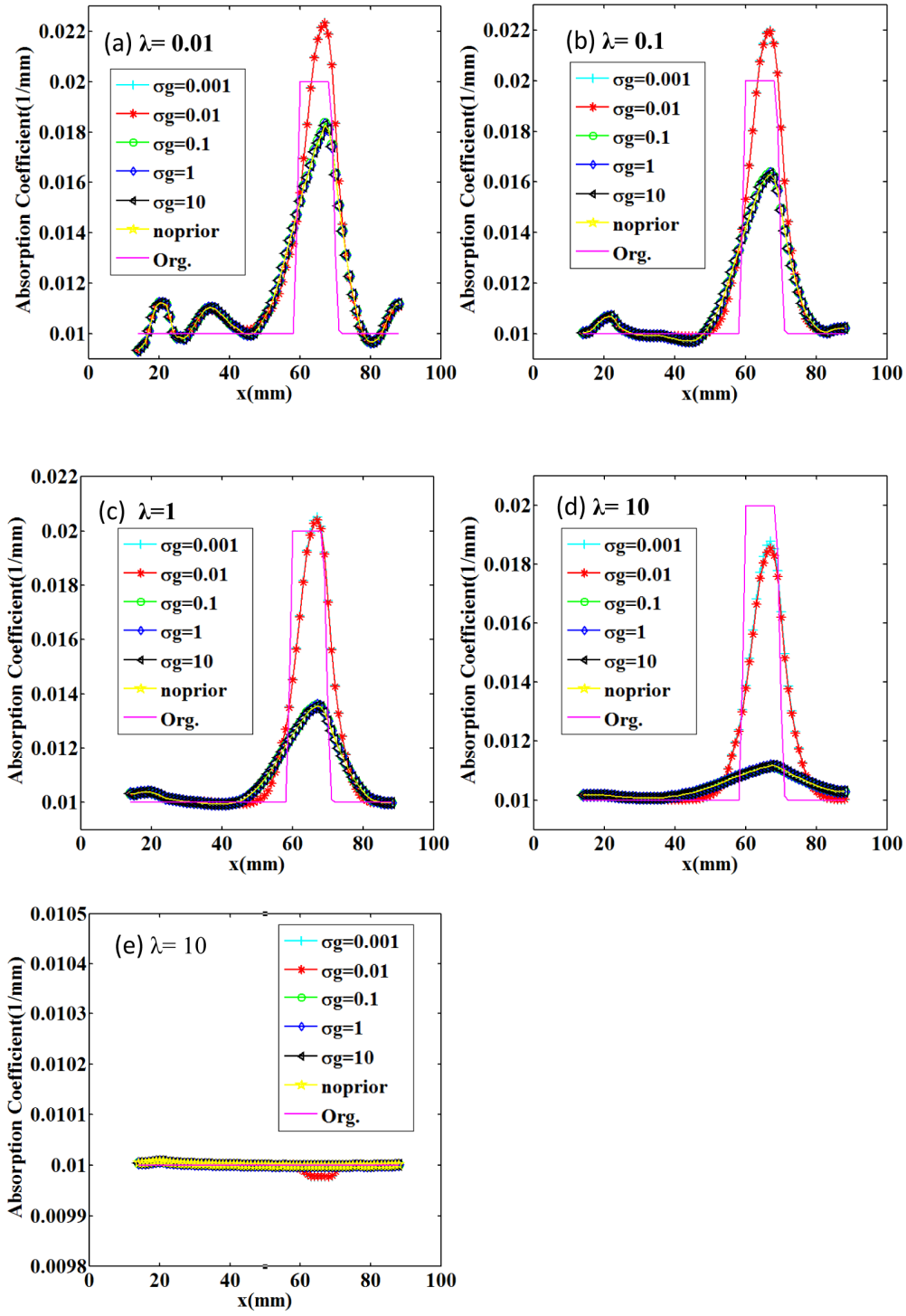

Fig. 3. (a)-(d) Profiles of the reconstructed absorption coefficient along the X-axis; (e) the reconstructed results of a negative control (no inclusion contrast) with λ = 10 and σg = 0.001, 0.01, 0.1, 1, 10.

#239691 Received 5 May 2015; revised 16 Jul 2015; accepted 17 Aug 2015; published 27 Aug 2015

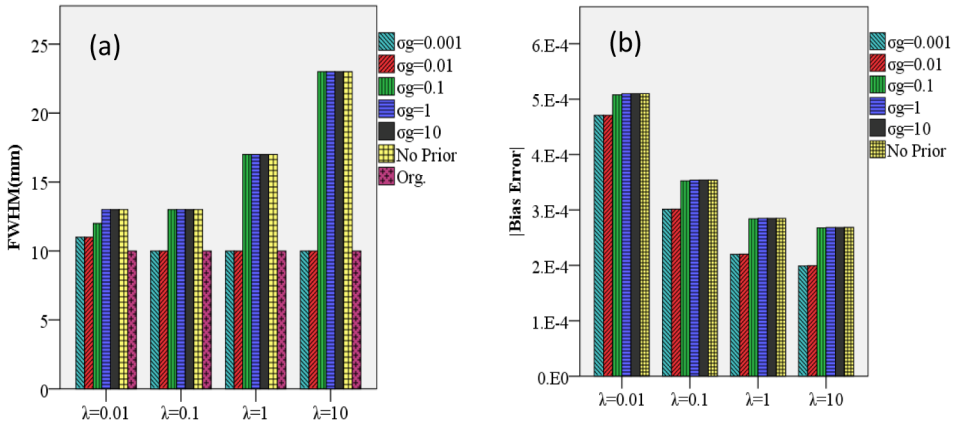

Fig. 4. (a) The full width at half maximum (FWHM) from the cross sectional profiles of the reconstructed inclusions; (b) the bias errors calculated for the reconstructed absorption coefficient images using no prior and DRI methods are shown.

3.2 Patient experiments

Based on the simulation results shown in Figs. 2–4, MRI guided NIRST images of a breast cancer patient were reconstructed with the DRI approach for $\lambda = 1$ and $\sigma_g = 0.001$. The patient was 61 years old, presented with a 20mm×27mm×33mm lump in the lower outer portion of the right breast. A modified radical mastectomy was subsequently carried out 1 day after the imaging session, and surgical pathology confirmed the lump was a low grade invasive ductal carcinoma.

Figure 5 shows MR images of this subject. The left image (a) displays the Nirview, 3D surface rendering from the T1 image volume where the fiber locations are evident from the tissue depressions of the breast surface and the fiducial markers. The middle image (b) shows a representative MR image slice from the standard T1 sequence. The tumor was not localized in this view but the fibroglandular (center, dark part) and adipose (bright) tissue compartments are readily visible. The right image (c) is a DCE-MR image. The lesion displayed wash in/wash out contrast enhancement kinetics and was bright in this image data. The contrast of the grey scale value of the tumor to surrounding normal tissues was approximately 1.4.

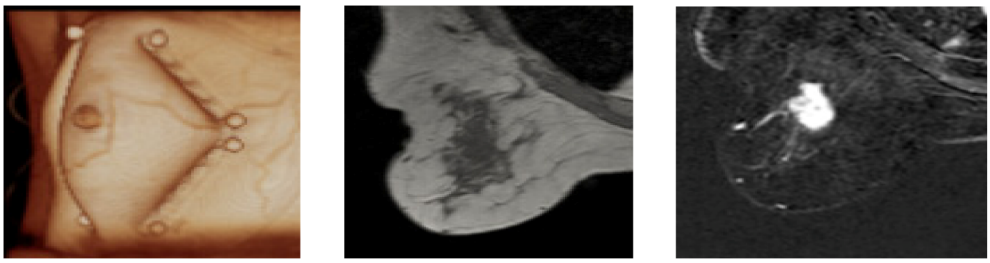

(a) 3D **(b) T1** **(c) DCE**

Fig. 5. MR images from a patient with a malignant lesion (20mm×27mm×33mm) seen on DCE MRI. (a): Screenshot of the Nirview 3D surface rendering of the T1 MRI. Fiducial markers and fiber bundle positions are shown; (b): Standard T1 image; and (c): Dynamic contrast-enhanced MRI.

Figure 6 shows reconstructed HbT images overlaid on T1 images in three planes of x = –100.0, y = –19.8 and z = –26.6, respectively. The HbT images were reconstructed with $\lambda = 1$ for both no priors and DRI methods ($\sigma_g = 0.001$ was used for DRI). Though the segmentation

#239691 Received 5 May 2015; revised 16 Jul 2015; accepted 17 Aug 2015; published 27 Aug 2015

is not required for our proposed approach, to validate the accuracy of the reconstructed tumor site, we compared its results to segmented images as references which are shown in Fig. 6(a) where the tumor was segmented from the T1 and DCE images in these planes [29]. Visualization thresholds were chosen to suppress the optical backgrounds. The optical images reconstructed with both no priors (b) and DRI (c) exhibited good agreement on tumor location relative to the segmented images. The estimated HbT in the tumor region was higher than the surrounding normal tissue, and suggested that the tumor was malignant. The recovered HbT contrast of the tumor to the normal surrounding tissue reconstructed by no priors and DRI was 2.4 and 3.6, respectively. Relative to no priors, tumor size reconstructed by DRI was much closer to the segmented size from DCE-MR in all three planes. The average optical image size differences relative to the segmented tumor from DCE-MRI were 18% and 6%, for the no-prior and DRI approaches, respectively.

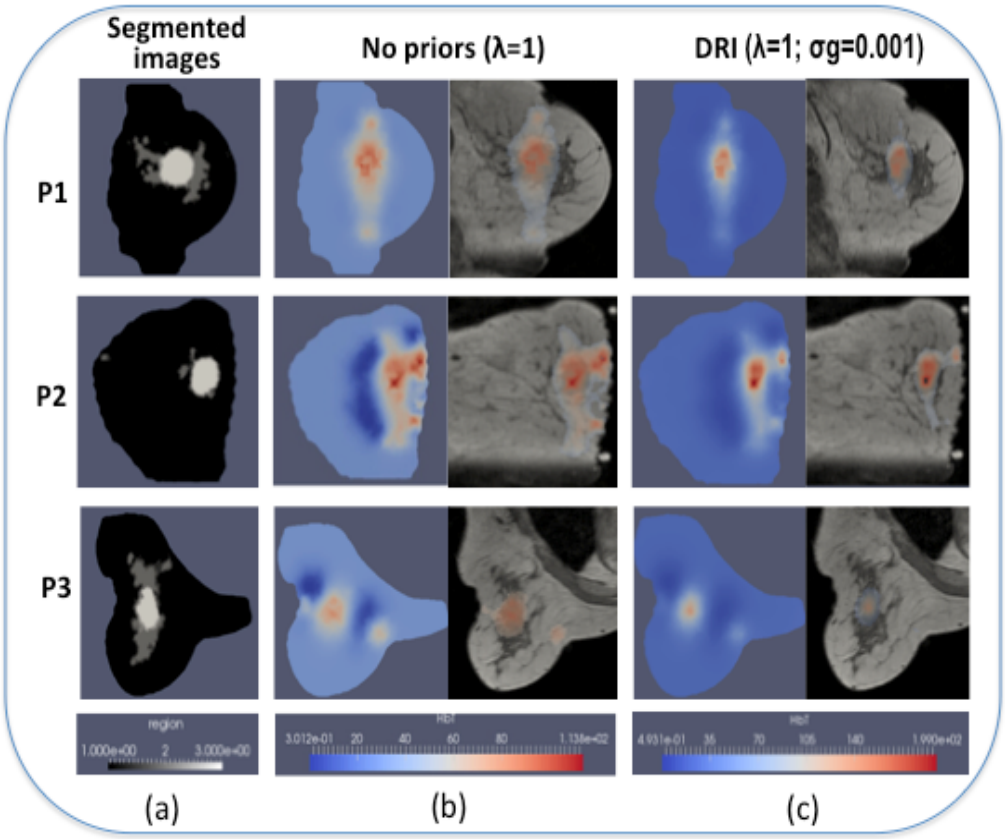

Fig. 6. The reconstructed HbT images overlaid in three planes with x = −100.0, y = −19.8 and z = −26.6 respectively. (a) Segmented images from corresponding T1 and DCE images. Optical images reconstructed by no priors; (b) and DRI with $\lambda = 1$ and $\sigma_g = 0.001$ (c), respectively.

4. Discussion

In this work, a direct regularization approach was implemented and evaluated and the omparisons with no-prior results demonstrated the notable advantages. Previous studies have shown that regularization based on high resolution structural information can provide a more stable and accurate NIRST solution [6–10]. For example, in Ref.6, grayscale values from the anatomical image were used to manually segment specific tissue types, and separate regularization parameters were implemented into the image reconstraction for each region using these values. Relative to this methold, DRI does not require image segmentation or ROI

#239691 Received 5 May 2015; revised 16 Jul 2015; accepted 17 Aug 2015; published 27 Aug 2015

selection, and implementation of its regularization matrix is implicitly encoded by a weight function which has an exponential distribution similar to a diffusion kernel, which matches the light diffusion process. While the formulations may be similar, the underlying rationale for the weight functional in DRI is different than the method in Ref. 6.

In order to obtain optimal image reconstruction, two parameters in the DRI method must be carefully selected. One is the well-known regularization parameter or weight coefficient, λ, and the other is the parameter, σ_g, introduced through the DRI regularization matrix. For the no prior method, noise can be efficiently suppressed by increasing the value of λ, but at the cost of sacrificing quantitative accuracy of the reconstructed image (higher bias error). In the DRI approach, when σ_g is large, as λ increases more weight is given to the prior information, accordingly, and the discrepancy between the prior information and the solution becomes smaller at the cost of larger differences between the model predictions and observations, whereas, when σ_g is small and λ is large, a balanced trade-off between model error and prior error is found; thus, the reconstructed image yields high spatial resolution and quantitatively accurate optical property values, simultaneously. These results indicate that λ needs to be in the range of 1 to 10, whereas the value of the σ_g is ideally much smaller, below 0.01, to attain proper balance between stability and accuracy. The negative control further proved that the DRI approach achieves image reconstructions compatible with model error reduction and prior information. In addition, the DRI method required fewer iterations to achieve convergent solutions compared to the no prior cases.

One important advantage of DRI is that the gray value is normalized (to the normal tissue), and the choice of σ_g is related to the contrast of the target (tumor) to the background (normal tissue). The reconstructed tumor to normal tissue contrast does not change significantly if the absolute gray-scale values shift up/down. In the numerical simulations presented above, the contrast in gray values within the inclusion relative to the background was selected to be 1.6, but the reconstructed results with other gray value contrasts exhibited the same trends (not shown in this paper), and the source and detector geometry did not affect the behavior of the reconstructed results.

The method in Ref.6 requires the reconstructed tissue to be composed of at least two compositions and the segmentation of these compositions into *N* components. In the DRI methodology introduced here, tissue is treated as a "continuum" in which the intensities in the input image are used as parameters to encode the regularization matrix implicitly. Fundamentally, this strategy creates a very different approach because the influences of segmentation errors and biased human input are eliminated, and no prior classification of tissues is necessary.

Although this work is focused on DCE-MRI as the source of the coregistered anatomical images for NIRST, the DRI approach is general and could be adapted to other high resolution anatomical images for guiding functional imaging modalities which require inversion similar to NIRST. For example, the anatomical images from CT could be combined with functional imaging modalities such as florescence optical tomography or bioluminescence tomography, through DRI.

The implicit assumption in DRI is that the gray scale anatomical image contains structural information which should influence the NIRST parameters, which is plausible for blood-based contrast such as hemoglobin. However, recovery of water, lipid and scattering values may not directly correlate with the types of gray scale structures evident on DCE-MRI. Utilizing a range of MRI scans selected to better map these parameters may be possible. For example, diffusion MRI could potentially best match with water images from NIRST, and T1 MRI might best match with lipids and scattering parameters. Thus, multiple DRI regularizations could be associated with multiple NIRST parameters and is an approach that requires further study to determine its advantages.

#239691 Received 5 May 2015; revised 16 Jul 2015; accepted 17 Aug 2015; published 27 Aug 2015

5. Conclusions

A direct inversion matrix regularization approach from coregistered anatomical images has been proposed and studied for MRI-guided NIRST. In this new methodology, the gray-scale image information from coregistered DCE-MRI is encoded directly into the inversion matrix regularization during NIRST image reconstruction without any requirements for user intervention such as image segmentation. Simulation results produced NIRST images that were significantly improved in terms of their qualitative and quantitative accuracy, as well as their robustness, when the associated regularization parameters were chosen appropriately. The method was also tested on *in vivo* breast data acquired by our combined NIRST/MRI imaging system. Compared to the standard "no priors" diffuse recovery, the contrast of the tumor to the normal surrounding tissue increased from 2.4 to 3.6, and the difference between the tumor size segmented from DCE-MRI and the reconstructed optical images decreased from 18% to 6%.

Acknowledgments

The authors acknowledge the funding support from the National Natural Science Foundation of China (61475115), Tianjin Municipal Government of China (14JCQNJC14400), and from the United States National Institutes of Health grant R01CA069554.

#239691 Received 5 May 2015; revised 16 Jul 2015; accepted 17 Aug 2015; published 27 Aug 2015